Applied Mathematical Modelling 77 (2020) 439–455

Contents lists available at ScienceDirect

Applied Mathematical Modelling

journal homepage: www.elsevier.com/locate/apm

Determination of Young modulus by using Rayleigh waves

M.T. Cao-Rial[a], C. Moreno[b], P. Quintela[c,d,*]

[a] Departamento de Matemáticas, Universidade da Coruña, Spain
[b] Departamento de Estadística, Investigación Operativa y Cálculo Numérico, Universidad Nacional de Educación a Distancia, Spain
[c] Departamento de Matemática Aplicada, Universidade de Santiago de Compostela, Spain
[d] ITMATI. Technological Institute for Industrial Mathematics, Campus Vida, Santiago de Compostela 15782, Spain

ARTICLE INFO

Article history:
Received 29 November 2018
Revised 17 July 2019
Accepted 23 July 2019
Available online 29 July 2019

Keywords:
Material properties
Non-destructive testing
Rayleigh waves
Finite element method
Young modulus

ABSTRACT

The aim of this work is to provide a non-destructive testing technique to obtain the physical properties of a given material, based on a series of images, obtained through a non-invasive procedure, that capture the experimental propagation of a Rayleigh waves packet travelling through it, and allowing us to obtain the phase velocity of the waves packet. The proposed procedure involves a minimization technique that requires the numerical simulation of the travelling waves to obtain the optimal material parameters. Numerical results are compared with experimental data to validate the procedure.

1. Introduction

Techniques for material characterization are classified as non-destructive testing (NDT) and destructive testing (DT). Under destructive techniques, the tested material or product cannot be used again. Besides, the destruction of the test object usually makes this type of test more costly, and can not be applied to structures already in operation. On the contrary, non-destructive testing techniques are specific procedures whereby the service ability of materials or components is not impaired by testing process. These are, therefore, more suitable for testing structures or mechanical pieces and they are proposed as material characterization techniques in many bibliographic works (see [1] and references therein).

The need to characterize elastic material properties is not new, and many authors have proposed different experimental methods alone or combined with numerical methods to achieve this goal. Back in the sixties of the last century, Fraser and Lecraw [2] proposed an experimental technique whereby the elastic and anelastic properties of a small sphere can be measured both as a function of its resonant frequencies and temperature by means of a transducer/receiver. Later on, in [3] resonant ultrasound spectroscopy was used for the determination of the elastic moduli of materials which were optimized by a fixed point iteration method and FEM.

Also, ultrasonic tests have been widely used to characterize a material and several wave generation and measuring techniques have been developed throughout the years to this end. Indeed, in the nineties, several approaches have been proposed for calculating the dynamic elastic moduli of concrete materials from wave velocities. For example [4–7], measured longitudinal and Rayleigh wave velocities by using different methods (P-wave transducers, impact generated waves, etc),

* Corresponding author. at: Departamento de Matemática Aplicada, Universidade de Santiago de Compostela, Spain
E-mail addresses: teresa.cao@udc.es (M.T. Cao-Rial), cmoreno@ccia.uned.es (C. Moreno), peregrina.quintela@usc.es, peregrina.quintela@itmati.com (P. Quintela).

https://doi.org/10.1016/j.apm.2019.07.051
0307-904X/

while measurements of the Rayleigh wave velocity and the aspect ratio of the elliptical trajectory amplitudes have been used in [8] to obtain the elastic constants of isotropic linear materials. In this case, such wave parameters were obtained by using an optical heterodyne interferometer that allows the point-like detection of the two components of the wave at the same point.

More recently, in [9] a new method is proposed for calculating the dynamic elastic constants of an anisotropic plate from measurements of the impact-echo resonance and Rayleigh wave velocity, while in [10] the authors combine experimental and numerical data to simultaneously determine the mechanical properties and damage parameters in multilayered composite plates.

The study of Rayleigh (and Lamb) waves propagation plays a key role in this ultrasonic tests so many authors have studied their properties and propagation through many different materials. The literature in this field is so vast that we cite here just a couple of the more recent or relevant works, like [11–13], or [14–16] and the references therein.

But not only linearly elastic materials need to be characterized, many efforts have been devoted to the characterization of other materials like bone [17], ice [18] or composites [19], for example.

Non-destructive testing, and in particular ultrasonic tests, are also frequently used to detect damage in a given structure, so that once the material properties are properly established, inverse problems can be used to determine the existence (or absence) of defects and even its location, see for example [20,21] and the references therein.

Regarding the numerical simulation of wave propagation, several methods can be found in the literature. For example, in [22,23], the discrete element numerical method (DEM) is described to simulate the propagation of acoustic emission waves, while in [24] the particle numerical model is applied to characterize the ultrasonic wave propagation in disorder materials.

In this work, we will focus on a particular technique, based on ultrasonic tests combined with numerical simulation, which can provide important diagnostic for microstructural properties of the piece or structure analyzed. The correct identification of the material parameters of interest as long as numerically reproducing the experiment characteristics is key to use numerical simulation as a reference tool to decide whether a structure built with that material is damaged or not. Therefore, these are two crucial steps that will be addressed in this work. The experimental results presented here have been obtained through image processing of the deformed upper surface of a prismatic structure[1] when a wave packet is travelling through, so only their velocity can be used for comparison. Nevertheless, the combination of these experimental results with numerical simulations and optimization procedures allow us to accurately determine the Young modulus of the elastic material, and numerically reproduce the experimental results, so that, detection of damage in the structure would also be possible. The authors continue here the work started in [25] where a first approach to material characterization was presented. In particular, in [25] the comparison between numerical simulation and experimental results would indicate if the material parameters considered where accurate or not, but no optimization procedure was developed in order to obtain the correct values. The optimization procedure presented in this work provides robustness to the material characterization process.

The overall plan for the paper is the following. First we will present the mathematical model for Rayleigh waves propagation and an analysis of the experimental data, corresponding to a five-pulse waves packet, that will be used for comparison on semi-infinite plates. Then, we will obtain the suitable boundary and initial conditions that will allow us to numerically reproduce the experimental wave packet and we present some preliminary numerical results obtained with tentative material data, that will reveal the need to characterize the material parameters more accurately. Therefore, the last part of the paper is devoted to present the optimization procedure that leads to said characterization and the numerical results obtained afterwards.

More precisely, the outline of the paper is as follows. First, in Section 2, we summarize the rigorous deduction of the theoretical expression corresponding to a specific Rayleigh wave, which will be somehow modified to reproduce the wave packet. Next, in Section 3 we analyze the experimental process and the provided data for the propagation of a wave packet, and we describe the procedure to obtain a Gaussian-like function that represents the variation in the wave amplitude. Said function, combined with the boundary conditions deduced in Section 2 will allow us to define the suitable boundary and initial conditions to numerically reproduce the experiment, where the amplitude of the waves is not constant (transient regime instead of harmonic). This model for the wave packet will be presented in Section 4. Then, in Section 5 we present the numerical results for the provided material data, which lead us to the need of optimizing the elastic parameters values. The optimization procedure is presented in Section 6, where we combine the experimental data of the wave packet propagation with numerical simulations to develop a methodology allowing the obtention of the Young modulus of the involved material. Numerical results with the optimized material parameters are also be presented in this section.

2. Mathematical model for Rayleigh waves

We consider a semi-infinite elastic body whose vertical middle section, Ω, is the semi-infinite domain in the plane Oxy given by $(0, +\infty) \times (-\infty, 0)$.[2] Its boundary, Γ, splits into two disjoint parts: $\Gamma_D = [x \equiv 0]$, where the displacements are imposed, and $\Gamma_N = [y \equiv 0]$, where the body is free. Let $[0, T]$ be the time interval of interest.

[1] In this work we will refer to such structure as plate, even though its mathematical treatment will not be that of plates.

[2] The whole body will therefore be $\Omega \times (-\infty, +\infty)$. By abuse of language we will refer to this body as plate, and we will focus on studying the behaviour of Rayleigh waves only in its vertical middle section Ω.

Due to Rayleigh waves properties, we can assume that the data verify the plain strain assumptions, so the three-dimensional elasto-dynamic problem is equivalent to the corresponding two-dimensional plain strain problem posed over Ω. Let $\boldsymbol{u}(x, y, t)$ denote the displacement field and u_α its components, $\alpha \in \{1, 2\}$. The components of the linearized strain tensor, $\varepsilon_{\alpha\beta}(\boldsymbol{u})$, are related to the stress tensor, $\sigma_{\alpha\beta}(\boldsymbol{u})$, through Hooke's constitutive law for elastic materials, being E its Young modulus and ν its Poisson coefficient. Under plane strain assumptions, the behavior of the plate is governed by:

- The equilibrium equation

$$\rho_0 \ddot{\boldsymbol{u}} - \mathrm{Div}\boldsymbol{\sigma} = 0 \quad \text{in} \quad \Omega, \tag{1}$$

  where ρ_0 is a positive real number representing the mass density of the material.
- The Dirichlet boundary condition

$$\boldsymbol{u} = \boldsymbol{u}^D \quad \text{on} \quad \Gamma_D, \tag{2}$$

  where $\boldsymbol{u}^D = (u_\alpha^D)$ is the imposed displacement on Γ_D.
- The free boundary condition

$$\boldsymbol{\sigma n} = 0 \quad \text{on} \quad \Gamma_N, \tag{3}$$

  where $\boldsymbol{n}$ is the unit outward normal to the boundary.
- The conditions at infinity that model one plate vibrating with a superficial wave on the whole structure:

$$\lim_{y \to -\infty} \boldsymbol{u}(x, y, t) = 0, \quad \boldsymbol{u} \text{ periodic with respect to } x. \tag{4}$$

To complete the model, we impose the following initial conditions, that are assumed to be compatible with the previous boundary conditions:

$$\boldsymbol{u}(x, y, 0) = \boldsymbol{u}_0(x, y), \quad \dot{\boldsymbol{u}}(x, y, 0) = \boldsymbol{v}_0(x, y), \quad (x, y) \in \Omega. \tag{5}$$

A suitable choice of the imposed displacement, $\boldsymbol{u}^D$, gives a Rayleigh wave as solution of (1)–(4). In order to properly define $\boldsymbol{u}^D$ we introduce the following parameters. Let k be the wave number, ω the angular frequency, L the wavelength and c_l and c_t the longitudinal and transversal wave propagation velocities, respectively; let us recall that these magnitudes are related by (see [14]):

$$k = \frac{2\pi}{L}, \quad \omega = c_t k \xi, \quad c_t^2 = \frac{E}{2\rho_0(1+\nu)}, \tag{6}$$

being ξ the only real root in the interval (0,1) of the equation

$$\xi^6 - 8\xi^4 + 8(1+2\alpha)\xi^2 - 16\alpha = 0, \text{ with } \alpha = 1 - \frac{c_t^2}{c_l^2} = \frac{1}{2(1-\nu)}. \tag{7}$$

The imposed condition on the vertical boundary Γ_D at each time t is:

$$\boldsymbol{u}^D(y, t) = (a_1(y)cos(\omega t), a_2(y)sin(\omega t)), \tag{8}$$

with

$$a_1(y) = -(2 - \xi^2)\eta_t e^{\eta_t y} + 2\eta_t e^{\eta_l y}, \tag{9}$$

$$a_2(y) = (2 - \xi^2)k e^{\eta_t y} - \frac{2}{k}\eta_t \eta_l e^{\eta_l y}, \tag{10}$$

being

$$\eta_l = k\sqrt{1 - \xi^2(1-\alpha)}, \quad \eta_t = k\sqrt{1 - \xi^2}. \tag{11}$$

Therefore, the solution of the posed mathematical problem (1)–(5) corresponds to a Rayleigh wave travelling in the x–direction given by (see [14]):

$$\boldsymbol{u}^R(x, y, t) = (a_1(y)cos(kx - \omega t), -a_2(y)\sin(kx - \omega t)), \tag{12}$$

and the initial conditions in (5) would be

$$\boldsymbol{u}_0(x, y) = \boldsymbol{u}^R(x, y, 0), \quad \boldsymbol{v}_0(x, y) = \dot{\boldsymbol{u}}^R(x, y, 0), \quad (x, y) \in \Omega. \tag{13}$$

The methodologies to numerically solve the above model are presented in [26] and will not be discussed here.

The obtention of expression (12) corresponds to an infinite plate vibrating with a Rayleigh wave. Nevertheless, when we try to generate just a Rayleigh wave packet in a plate at rest, like those generated by a piezoelectric located at $x = 0$, two major challenges must be addressed: on one hand, the amplitudes of the waves in the packet are not constant, which requires an adequate modification of the boundary condition on Γ_D; on the other hand, how to choose the initial conditions so that they are compatible with the boundary ones while keeping the plate as close as possible to being at rest.

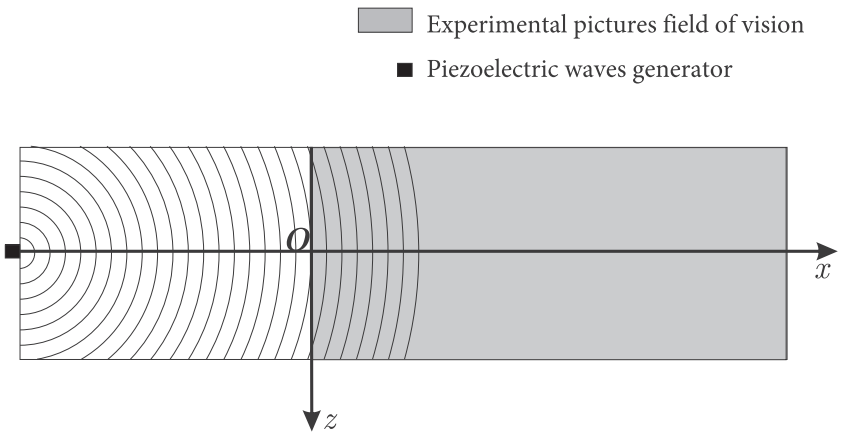

Fig. 1. Schematics of the surface of the experimental plate and the field of vision for the pictures (gray shaded surface), laying on the $y = 0$ plane.

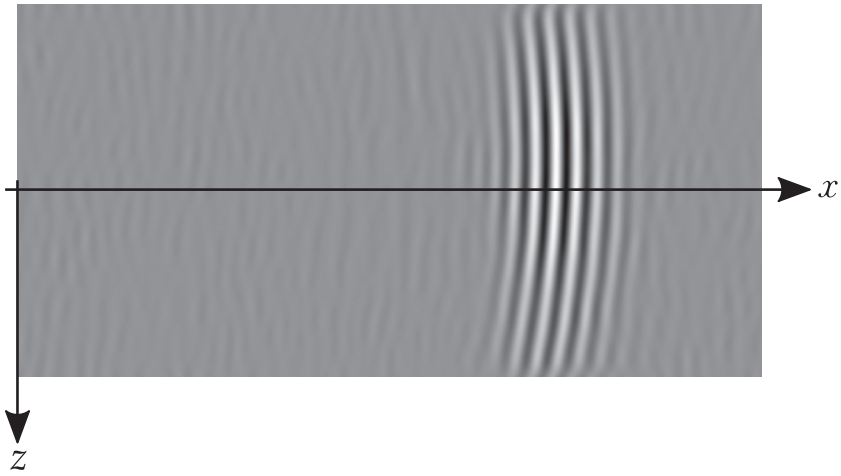

Fig. 2. Experimental image at time step $t_{110} = 2.2 \times 10^{-5}$ s on the upper boundary of the plate, $y = 0$.

3. Experimental process and treatment of data

In this section we will analyze the designed experimental process and discuss the several issues that arise when we try to compare the measured variables with the numerical simulation results of the previous mathematical model.

3.1. Analysis of the experimental process

The experimental process that we will use in this work was designed by the Optical Metrology Research Group of the Applied Physics Department at the Universidade de Vigo and the methodology is valid for any elastic material.

They used a piezoelectric system to generate a transient oscillation of Rayleigh waves on an aluminum plate and took pictures of the plate surface at 135 regular time intervals of 200 ns, what induce a time discretization $t_i = 2i \times 10^{-7}$s, $1 \leq i \leq 135$. A scheme of the experiment is shown in Fig. 1. The interested reader can find a more detailed description of the experimental procedure for the generation of Rayleigh wavetrains in [27].

The field of vision for the pictures is a rectangle on the upper surface of the plate with dimensions $0.05535\,\text{m} \times 0.1107\,\text{m}$ in the OZX plane and the picture size is 512×1024 pixels. So for each time step/picture, t_i $1 \leq i \leq 135$, a matrix $D_i \in \mathcal{M}_{512\times1024}$ containing the values of the corresponding RGB value for each pixel shade of gray is obtained. Such values range from $0 \equiv rgb(0, 0, 0)$ (black) to $255 \equiv rgb(255, 255, 255)$ (white). These values are therefore non-dimensional, so this experimental procedure does not provide the actual amplitude of the waves. Nevertheless, after a suitable scaling, we will relate the shades of gray with the wave height on each pixel of the picture, so $D_i(n, j)$ represents in some way the measured wave height for time t_i, at the n-th pixel in the z-direction, $1 \leq n \leq 512$, and at the j-th pixel in the x-direction, $1 \leq j \leq 1024$. In the following, for the sake of simplicity and *"par abus de langage"* we will refer to the wave height when talking about the experimental RGB values in D. An example of such a picture at time step $t_{110} = 2.2 \times 10^{-5}$ s is shown on Fig. 2. In order to obtain just Rayleigh wavetrains the depth of the plate has to be much larger than the wavelength as explained in [28] where

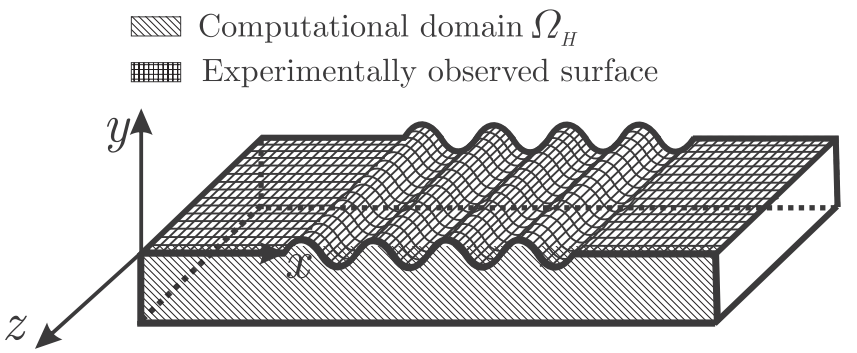

Fig. 3. Scheme of the half of the three dimensional domain that corresponds to $z \leq 0$, this is, $(0, 0.1107) \times (-0.030, 0) \times (-0.027675, 0)$, half of the experimentally observed surface $(0, 0.1107) \times \{0\} \times (-0.027675, 0)$ (gridded), and the computational domain at $z = 0$, this is, $(0, 0.1107) \times (-0.030, 0) \times \{0\}$ (lined).

the details of the experiment can be consulted. That is why the experimental plate considered has depth 30 mm. Therefore, the three dimensional domain considered is $(0, 0.1107) \times (-0.030, 0) \times (-0.027675, 0.027675)$.

The tentative experimental data for the material and wave characteristics were:

- Material density: $\rho_0 = 2790$ kg/m^3.
- Young modulus: $E = 7.263e10$ Pa (measured with a 5% error margin).
- Poisson coefficient: $\nu = 0.34$. Therefore, $\xi = 0.9335$.
- Frequency: $f = 1$ MHz. Therefore, the angular frequency is $\omega = 2\pi f = 6283185.31$ rad/s.

With these data, the velocities and wavelength are

$$c_t = 3.1167e+03 \text{ m/s}, \quad c_l = 6.33e+03 \text{ m/s},$$

$$L = 0.0029 \text{ m}.$$

3.2. Experimental data post-process

As one can see in Fig. 2, the experimental pictures taken represent only the behavior of the plate on its upper surface, that is the plane $y = 0$. This means that the comparison between numerical and experimental results can only be made on a line, in practice, which corresponds to $z = 0$, $y = 0$, that is x-axis in the midmost vertical section of the plate (see Fig. 3).

In order to obtain representative values on this line from the experimental data, we propose to compute the mean of the values on several central rows of the experimental matrix for each time step. Therefore, from the experimental values, $D_i(n, j)$, corresponding to the color height on the upper surface at time t_i for the j-th pixel on the abscissas axis x, the matrix $d(i, j)$ actually used for comparison with the corresponding numerically computed values for $u_2(x_j, 0, t_i)$, with $x_j = h(j - 1/2)$, $1 \leq j \leq 1024$, and h the distance between two consecutive pixels, will be calculated as

$$d(i, j) = \frac{1}{2n_r + 1} \sum_{n=256-n_r}^{256+n_r} D_i(n, j), 1 \leq j \leq 1024, \ 1 \leq i \leq 135,$$

being $2n_r + 1$ the number of central rows considered; in the present experiment, the choice of $n_r = 5$ gave good results.

Since the piezoelectric wave generation system has the peculiarity of producing Rayleigh waves with variable amplitude, boundary condition (8) has to be modified to fit it to the wave amplitudes according with the experiment. Therefore, we will need to figure out a function that, multiplied by expression (12), accurately represents the variation of the experimental wave amplitudes, which is known to have Gaussian-like form (see Fig. 4).

Our efforts on the remaining of this section will be devoted to compute such Gaussian function.

As we explained on the previous subsection, only the experimental data of the local maxima can be related to actual numerical displacements. We will consider that the wave packet consists of n_l wave cycles as shown in Fig. 4; for this experiment we consider $n_l = 7$, assuming that the vibrations that appear before and after the wave packet are the result of the image treatment and the noise on the measurements. Notice that n_l must be taken odd to incorporate the symmetry of the wave train with respect to the absolute maximum. Given an instant, t_i, and known the position of the absolute maximum, we also know the position of the other $n_l - 1$ maxima. Let us denote by $p_i(l)$ the pointer giving the position on $d(i, j)$ of the l-th relative maxima $(1 \leq l \leq n_l)$ at time t_i, and the corresponding values for the vertical wave height are denoted by $m_i(l)$, so (see Table 1)

$$m_i(l) = d(i, p_i(l)), \ 1 \leq l \leq n_l.$$

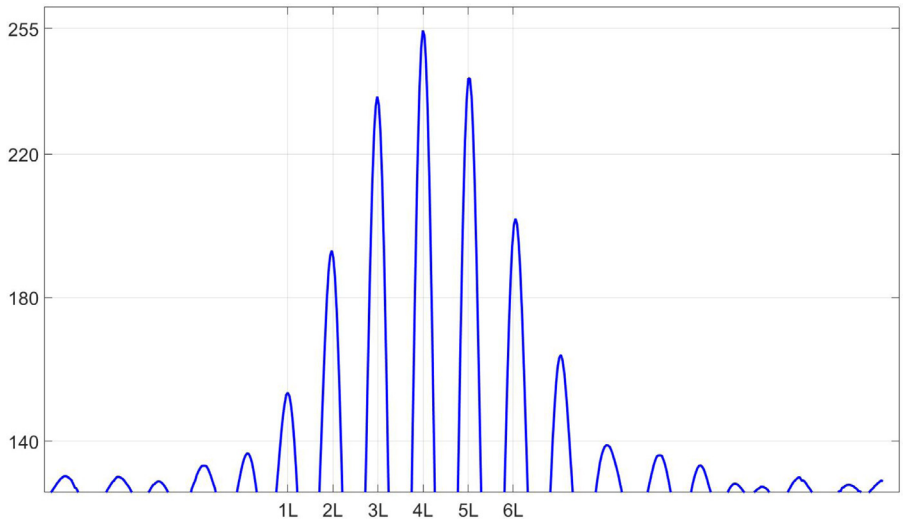

Fig. 4. Detail of the experimental data $d(110, j)$ at $y = 0$ and $z = 0$. The abscissas axis represent the x direction and the ordinate the RGB value for each pixel.

Table 1
Sample and position of the data for time t_{110} considering $n_l = 7$.

$lL\,[m]$	$p_{110}(l)\,\sharp$	$m_{110}(l)$ RGB
L	658	153.4545
2L	685	193.0909
3L	713	236.0000
4L	741	254.4545
5L	769	241.0909
6L	798	202.0000
7L	826	164.0000

Notice that at the relative maxima, the height on each pixel corresponds, except for a scaling factor, to the experimental vertical displacement $u_2(x_j, 0, t_i)$.

3.2.1. Wave packet Gaussian profile

We assume that the Gaussian function describing the shape of the wave packet takes the form

$$g(x, \tau) = 255e^{\frac{-(x-C_R\tau-b)^2}{2s^2}}, \tag{14}$$

being $\tau = t - \delta$ a fictitious time allowing us to incorporate a delay, δ, to the wave packet movement on the plate surface. As we will see in the next section, this delay facilitates to properly mark the initial instant for the numerical test so that the plate is practically at rest at that moment. In expression (14), b represents the mean, s the standard deviation and $C_R = \frac{L}{T_0}$ the wave phase velocity, with L its wavelength and T_0 its period. Both b and s will be computed observing the global behavior of the wave packet for all time, while C_R will be considered known for the time being. Indeed, with the tentative experimental data considered in Section 3.1 we get

$$C_R = \frac{L}{T_0} = Lf = 2909.48 m/s. \tag{15}$$

But these values were computed from tentative material data, so, we will try to obtain or at least approximate them, at each measuring time, as many as possible from the experimental data, like those showed in Table 1 for t_{110}.

Wavelength approximation. For each time step, t_i, $1 \le i \le 135$, we have data on 1024 equidistant points in the x-direction of the upper boundary of the middle section of the plate corresponding to the discretization points x_j. Given the field of vision for the pictures, the distance between two consecutive points is $h = 1.0821e-04$ m, and therefore $x_j = jh, 1 \le j \le 1024$. After a detailed analysis of the measured data, we can observe that relative maxima occur, approximately, each 28 points so, the distance between two consecutive maxima is 28 h m, and we can conclude, as first approach, that the wavelength is approximately $L = 0.0030$ m. In Section 6 we will use an optimization procedure to obtain a more accurate value for the wavelength.

Mean and standard deviation approximation. In the following we will focus on the approximation of parameters b and s of Eq. (14). They will be approximated by using the mean of the corresponding Gaussian profiles computed from the measured data at 135 instants, $t_i = 2i \times 10^{-7}$ s, $1 \le i \le 135$, computing for each one $b_i \simeq b(t_i)$ and $s_i \simeq s(t_i)$, being $b(t_i)$ and $s(t_i)$ the mean and the standard deviation of the wave package at time t_i.

Therefore, at time t_i, the sample to calculate the parameters of the Gaussian function, g, consists of the values $lL, 1 \le l \le n_l$, and their corresponding weights $m_i(l)$ (see Table 1). The sample size is

$$N_i = \sum_{l=1}^{n_l} m_i(l).$$

Its mean, b_i, and its variance, s_i^2, are

$$b_i = \frac{1}{N_i} \sum_{l=1}^{n_l} m_i(l) lL, \quad s_i^2 = \frac{1}{N_i} \left(L^2 \sum_{l=1}^{n_l} m_i(l) l^2 \right) - b_i^2.$$

Once computed the mean and variance for each time step, we compute the mean of all of them to obtain the final expression:

$$b = \frac{1}{135} \sum_{i=1}^{135} b_i, \quad s^2 = \frac{1}{135} \sum_{i=1}^{135} s_i^2. \tag{16}$$

From the experimental data provided, the values obtained were $b = 3.9642\mathrm{L}$, and $s^2 = 3.4665\mathrm{L}^2$. Therefore, the identification of all parameters for the Gaussian profile g is complete.

Fig. 6 shows a representation of the experimental wave packet together with the resulting Gaussian function at time t_{110}. As we can see, the approximation is not exact, which was expected since the experimental data are not completely symmetric. That is another reason why, in order to compute the errors, we will only use the absolute maximum of the experimental wave at each time which is much better approximated.

This lack of symmetry of the data can also be noted on the mean values for each time step, since theoretically it should be 4 L, while in practice is not; for example, for $n = 25$, $b_{25} = 3.9557\mathrm{L}$, while for $n = 110$, $b_{110} = 4.0378\mathrm{L}$.

Summarizing, from this postprocess of the experimental data, we can assume that the piezoelectric behaviour produces a Rayleigh wave package considering as boundary condition at Γ_D:

$$\tilde{\boldsymbol{u}}^D(y,t) = g(0, t-\delta)\boldsymbol{u}^D(y,t),$$

with $\boldsymbol{u}^D$ defined as in (8).

4. Mathematical modelling of the wave packet

In this section we present a mathematical model that allows to obtain a wave packet that replicates the behavior of the plate in the experiment. In particular, we will describe the obtention of appropriate fitting of boundary conditions matching the behavior of the wave packet induced by the piezoelectric and the identification of initial conditions close enough to zero but compatible with the imposed boundary conditions. First we will introduce the computational domain, then two subsections will be devoted to the boundary and initial conditions respectively, and finally we will present the whole model.

4.1. Computational domain

For the numerical simulation of the travelling wave packet, the first consideration to take into account is that the domain needs to be bounded. Besides, as we said before, solving the three-dimensional problem (1)–(5) is equivalent to solve a plain strain problem on the middle vertical section of an unbounded plate to simulate the propagation of the waves. Therefore, since Rayleigh waves are superficial and the area of vibration at each time is concentrated in a small part of the plate, a good approximation of the plain problem can be obtained by considering a bounded plate $\Omega_H = (0, H_x) \times (-H_y, 0)$, being H_x and H_y positive numbers and H_y large enough, for example $H_y = 0.02$ m. Let us recall that from the experimental plate, $H_y = 0.03$, but in order to reduce computational cost we can consider $H_y = 0.02$, because the displacements are null for points with $y \le -0.02$. The boundedness on the longitudinal direction x, which is also necessary for numerical purposes, might introduce reflection effects which must be avoided; nevertheless, based on the size of the experimental images (see Section 3.1), and since the waves in the experiment never reach the right boundary, we consider a plate 0.1107 m long, like in the picture field of vision. We will not care about its width, since we will be simulating just a vertical section of the plate.

4.2. Boundary conditions

In the domain Ω_H, two new boundaries appear, $\partial\Omega_H = \Gamma_D \cup \Gamma_N \cup \Gamma_D^1 \cup \Gamma_D^2$, with Γ_D^1 corresponding to $y = -H_y$, and Γ_D^2, corresponding to $x = H_x$, as shown in Fig. 5, for which we will also need to define their appropriate boundary conditions.

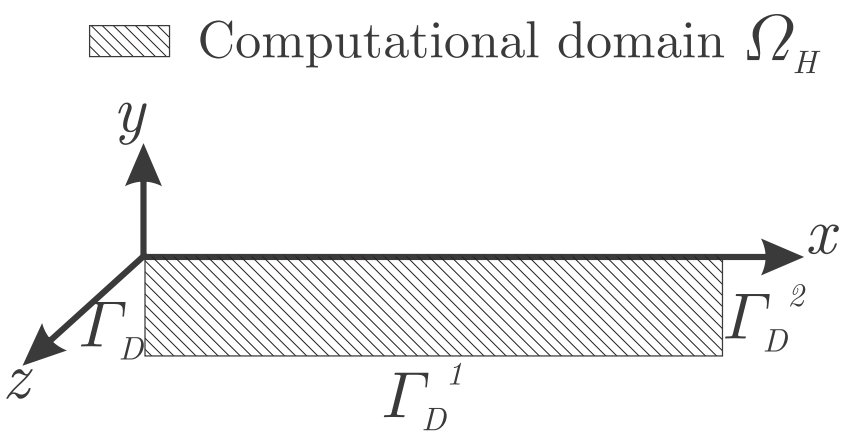

Fig. 5. Computational domain corresponding to the vertical section $z = 0$, $\Omega_H = (0, 0.1107) \times (-0.02, 0)$.

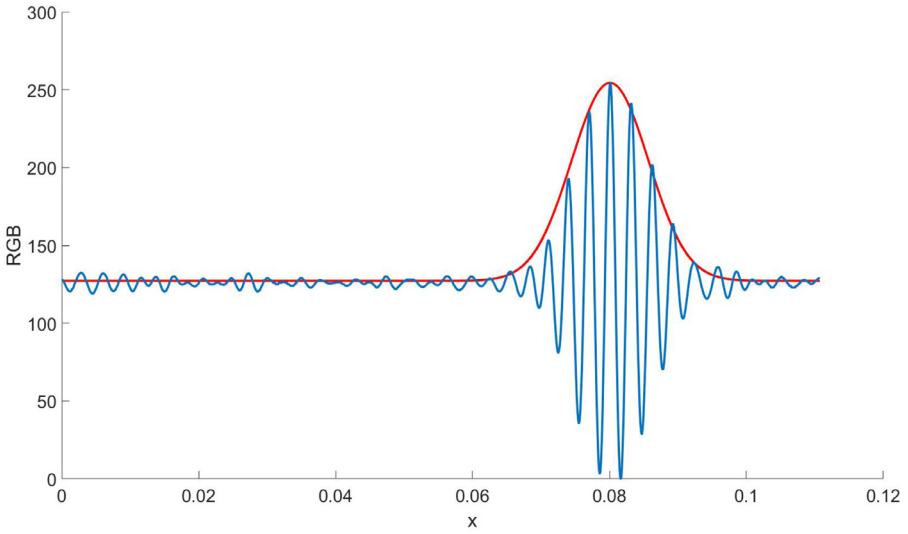

Fig. 6. Gaussian function and experimental wave at time step $t_{110} = 2.2 \times 10^{-5}$ s. The abscissas axis represent the x direction and the ordinate the RGB value for each pixel.

- On Γ_D, the boundary condition to be taken is essential since it must be able to reproduce the passage through this boundary of the wave train induced by the piezoelectric. For this reason, we will consider as boundary condition the one corresponding to the problem associated with Rayleigh waves, given by (8), but re-scaled to the Gaussian profile calculated in the previous section at $x = 0$. Also, in order to have the initial plate as close to the rest as possible, we will consider a delay, δ, in the Gaussian function (14); in particular, $\tau = t - \delta$, being $\delta = \frac{b+5L}{C_R}$ a good choice as it will be seen in the numerical results.
  Therefore, the boundary condition imposed on Γ_D is:

$$\boldsymbol{u}(y,t) = \hat{\boldsymbol{u}}^D(y,t) \text{ on } \Gamma_D, \tag{17}$$

being

$$\hat{\boldsymbol{u}}^D(y,t) = \hat{g}(t)\boldsymbol{u}^D(y,t), \tag{18}$$

with $\boldsymbol{u}^D$ given by expression (8), and

$$\hat{g}(t) = \frac{1}{255} g(0, t-\delta) = e^{-\frac{(C_R t - 5L)^2}{2s^2}}.$$

With the imposed delay, the maximum of the Gaussian function at time $t = 0$ is reached at $x^\star = -5L$, far enough from Γ_D, and it will move forward with time, while its value at $t = 0$ on this boundary is:

$$\hat{g}(0) = e^{-\frac{25L^2}{2s^2}} = 0.0272,$$

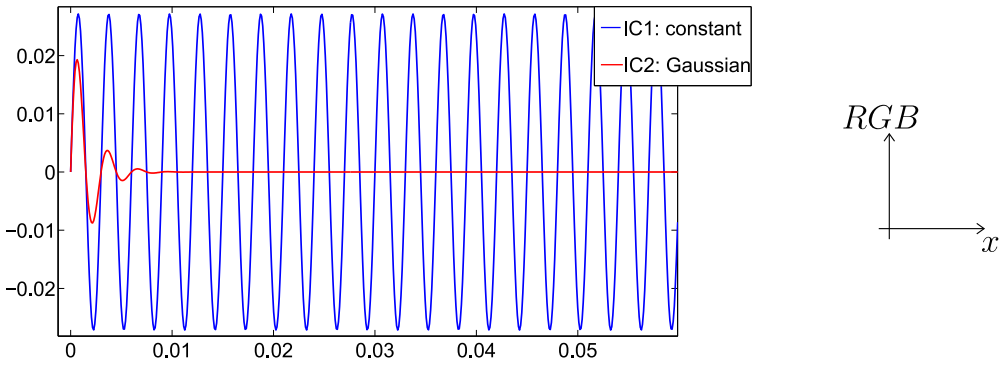

Fig. 7. Proposed initial conditions. The abscissas axis represent the x direction and the ordinate the RGB value for each pixel. (For interpretation of the references to color in this figure, the reader is referred to the web version of this article.)

small enough for imposing initial conditions compatible with boundary condition (17) and allowing the plate to remain almost at rest at $t = 0$.

- Since the Rayleigh waves travel only near the surface $y = 0$, a null Dirichlet condition is considered on Γ_D^1.
- On Γ_D^2 several boundary conditions could be assumed. The usual approach would be to consider an absorbing boundary condition to avoid reflection effects if the waves reach that area; nevertheless, the experimental wave packet does not reach that boundary in the time interval of interest so we could also consider a free surface condition or a null Dirichlet condition. Our choice is quite different; since it is recommended its compatibility with the initial condition, we will impose on this boundary a wave with constant amplitude, but small enough to avoid significant reflection.

Therefore, since we will consider two different possibilities for the initial conditions that entail different initial amplitudes on Γ_D^2, two boundary conditions also arise on Γ_D^2, both representing a wave with constant amplitude in time:

$$\boldsymbol{u}(H_x, y, t) = \tilde{\boldsymbol{u}}^D(y, t) \text{ on } \Gamma_D^2, \tag{19}$$

being $\tilde{\boldsymbol{u}}^D$ either

BC1:

$$\tilde{\boldsymbol{u}}^D(y, t) = \hat{g}(0)\boldsymbol{u}^R(H_x, y, t), \tag{20}$$

or

BC2:

$$\tilde{\boldsymbol{u}}^D(y, t) = \frac{1}{255} g(H_x, -\delta)\boldsymbol{u}^R(H_x, y, t), \tag{21}$$

depending on the initial condition considered (see Section 4.3).

4.3. Initial conditions

The initial conditions must be compatible with the necessary non-null boundary conditions at time $t = 0$ on Γ_D to generate the wave packet, but at the same time as close as possible to zero since actually the plate is initially at rest. We have considered two possibilities:

IC1: The initial conditions correspond to a Rayleigh wave $\boldsymbol{u}^R(x, y, 0)$ and its time derivative $\dot{\boldsymbol{u}}^R(x, y, 0)$ both re-scaled by the same factor $g(0)$ than the boundary condition on Γ_D as in (20):

$$\boldsymbol{u}(x, y, 0) = \hat{\boldsymbol{u}}_0(x, y), \;\; \dot{\boldsymbol{u}}(x, y, 0) = \hat{\boldsymbol{v}}_0(x, y) \;\; \text{in } \Omega_H, \tag{22}$$

where $\hat{\boldsymbol{u}}_0(x, y) = \hat{g}(0)\boldsymbol{u}^R(x, y, 0)$, and $\hat{\boldsymbol{v}}_0(x, y) = \hat{g}(0)\dot{\boldsymbol{u}}^R(x, y, 0)$, for all $(x, y) \in \Omega_H$. The result is a wave with constant amplitude over the whole plate at $t = 0$ (see blue line in Fig. 7).

IC2: The initial conditions correspond to those of the Rayleigh wave $\boldsymbol{u}^R(x, y, 0)$ and its time derivative $\dot{\boldsymbol{u}}^R(x, y, 0)$ both re-scaled by the value $g(0)$ of the Gaussian profile on each x this is, in (22) we consider:

$$\hat{\boldsymbol{u}}_0(x, y) = \frac{1}{255} g(x, -\delta)\boldsymbol{u}^R(x, y, 0) = e^{-\frac{(x-5L)^2}{2s^2}} \boldsymbol{u}^R(x, y, 0), \tag{23}$$

and

$$\hat{\boldsymbol{v}}_0(x, y) = \frac{1}{255} g(x, -\delta)\dot{\boldsymbol{u}}^R(x, y, 0) = e^{-\frac{(x-5L)^2}{2s^2}} \dot{\boldsymbol{u}}^R(x, y, 0), \tag{24}$$

for all $(x, y) \in \Omega_H$.

Note that for $x = 0$ the value of $\hat{\boldsymbol{u}}_0(0, y)$ is the same for both options and coincides with the imposed Dirichlet condition on Γ_D (see (18)) at the initial time. With the second option, IC2, the amplitude of the initial wave is not constant over the whole plate, but it decreases exponentially just like the Gaussian function so it will be closer to a plate initially at rest (see red line in Fig. 7). Also, option IC2 allows us to consider a much smaller boundary condition on Γ_D^2, corresponding to (21), which will prevent reflection on that boundary.

On Fig. 7 we can see graphically the difference between both initial conditions. The blue line represents IC1 (constant amplitude) and the red line IC2 (exponentially decreasing amplitude). Although theoretically the second option might seem better, the results obtained with both simulations did not present any significant differences.

4.3.1. Mathematical model

In the following we summarize the equations that model the Rayleigh wave packet travelling on a plate.

$$\rho_0 \ddot{\boldsymbol{u}} - \mathrm{Div}\boldsymbol{\sigma} = 0 \quad \text{in} \quad \Omega_H \times (0, T), \tag{25}$$

$$\boldsymbol{\sigma n} = 0 \quad \text{on} \quad \Gamma_N \times (0, T), \tag{26}$$

$$\boldsymbol{u} = \hat{\boldsymbol{u}}^D \quad \text{on} \quad \Gamma_D \times (0, T), \tag{27}$$

$$\boldsymbol{u} = \tilde{\boldsymbol{u}}^D \quad \text{on} \quad \Gamma_D^2 \times (0, T), \tag{28}$$

$$\boldsymbol{u} = 0 \quad \text{on} \quad \Gamma_D^1 \times (0, T), \tag{29}$$

$$\boldsymbol{u}(x, y, 0) = \hat{\boldsymbol{u}}_0(x, y), \quad \dot{\boldsymbol{u}}(x, y, 0) = \hat{\boldsymbol{v}}_0(x, y), \quad (x, y) \in \Omega_H, \tag{30}$$

with the data $\hat{\boldsymbol{u}}^D$, $\tilde{\boldsymbol{u}}^D$, $\hat{\boldsymbol{u}}_0$ and $\hat{\boldsymbol{v}}_0$ introduced in (18), (21) corresponding to BC2 boundary condition, and (23)-(24) corresponding to IC2 initial condition. The total interest time is $T = 2.7e - 5$ s.

5. Numerical results

For the numerical simulation with the finite element method a structured mesh consisting of 99425 nodes, 196608 triangular elements and 1025 points on the upper boundary, Γ_N, of the middle plane of the plate, Ω_H, is considered. If we take in consideration the length of the computational domain, 0.1107 m, the number of elements on the surface, 1024, and the approximate wavelength of 0.003 m, one can easily compute the number of elements per wavelength, which is about thirty. The elements are Lagrange $P1$ and for the time discretization an implicit method from the Newmark family, with parameters $\beta = 0.25$ and $\gamma = 0.5$, is used (see [29] for details on the numerical method). A time step $\Delta t = 2.e - 8$ s is considered.

Notice that for the comparison between experimental data (see Table 1 for time t_{110}) and numerical results, only an image for the deformation on the upper surface, that is on the boundary Γ_N, is available at each time from the experimental pictures. So, unfortunately, we cannot immediately relate the color height on each pixel with displacements on nodes. Nevertheless, according to Eq. (12), the vertical displacement of a node coincides with the corresponding pixel height when the tangential component of the displacement is null, which happens only on the pixels where the local maximum of the vertical amplitudes are reached. Therefore, only the measurements in these pixels will be considered to compare with the numerical results.

As we said in Section 4.2, the numerical simulation starts with a delay δ with respect to the time discretization of the experiment, in order to get a small initial condition. In the following numerical results of this paper we consider $\delta^\star = \frac{b+5L}{C_R}$ to start with, so we will have an initial wave amplitude of 0.0272 on Γ_D over the wave maximum amplitude of value 255 that is reached at $x^\star = -5$ L, external point to the computational domain and far enough from Γ_D. If we wish to use an initial condition closer to zero we could simply consider a bigger value for δ: for example, just taking $\bar{\delta}^\star = \frac{b+8L}{C_R}$ (with maximum at $\bar{x}^\star = -8L$), we get an initial amplitude of $9.7857e - 05$ m on Γ_D; however, this choice has a drawback, since the number of time iterations is increased due to the delay, and we can only compare the numerical data with the experimental ones once the wave packet has reached the positive x, and it will take longer the further away we start the simulation (it will require 150 additional time iterations for the second delay parameter). In the numerical tests carried out, no significant differences were observed for higher delays than $\delta^\star$.

With the material data introduced in Section 3.1, the comparison between numerical and experimental results showed good accuracy by approximating the amplitudes of the waves, but a significant gap on the wave packet position when time increases. Indeed, as one can see from Figs. 8 and 9, where the numerical simulation is compared with the first and last picture of the experiment respectively, the experimental wave (which is travelling with an unknown velocity C_R^E m/s) is

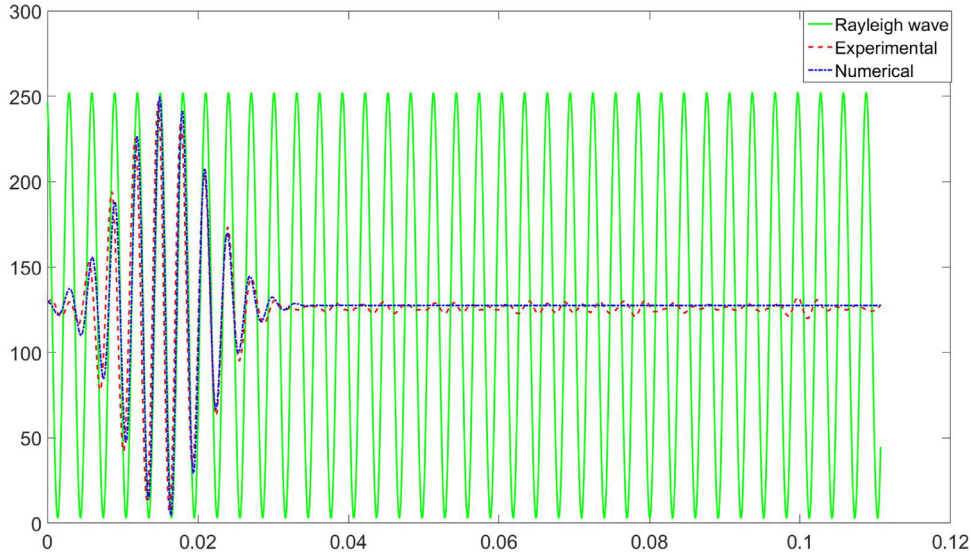

Fig. 8. Numerical and experimental wave packet comparison at the first comparison time $t_1 = 2 \times 10^{-7}$ s. The comparison of their profiles with respect to the Rayleigh wave is shown. The abscissas axis represent the x direction and the ordinate the RGB value for each pixel.

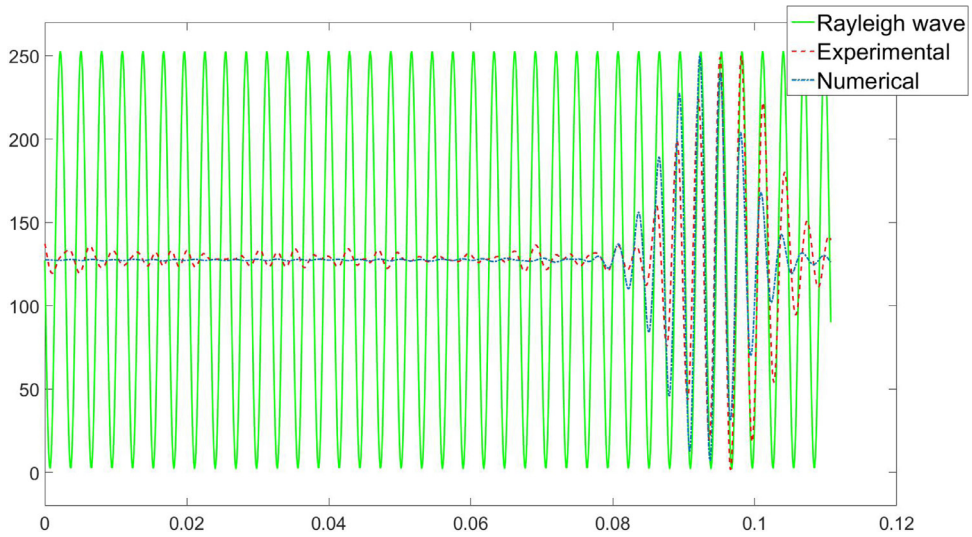

Fig. 9. Numerical and experimental wave packet comparison at time $t_{135} = 2.7 \times 10^{-5}$ s. The comparison of their profiles with respect to the Rayleigh wave is shown. The abscissas axis represent the x direction and the ordinate the RGB value for each pixel.

travelling faster than the numerical and theoretical Rayleigh waves who travel both with a velocity C_R^N m/s, whose value is obtained from the physical parameters provided by the company. There are two possible explanations for this discrepancy:

1. The time step between two consecutive pictures of the experiment might be bigger than $2.e-7$ s. This would mean that the comparison was not being made at the same instants. However, the accuracy on the specifications of the photography equipment made this explanation unlikely.
2. The accuracy of the Young modulus or Poisson coefficient values was not enough to obtain the real wave velocities.

Therefore, in the next Section we will focus on adjusting the values of the material parameters.

6. Data adjustment

Now, in order to obtain the correct parameters of the material, in particular the phase velocity of the experimental wave packet and the Young modulus E, we will use a minimization procedure. In the following we will present an algorithm that minimizes a suitable cost function to ensure that both wave packets (numerical and experimental) travel with the same

velocity. Said function will represent the 2-norm of the distance between the positions where the value of the amplitude of the numerical and experimental wave packet reaches its maximum over time.

6.1. Optimization algorithm

In this subsection we focus on obtaining the suitable cost function and present the algorithm to minimize it and to obtain more accurate values for the Young modulus.

6.1.1. Cost function

Let us consider that the numerical wave packet travels at C_R^N m/s, (magnitude computed from the physical parameters initially provided by the company), and that the observed velocity of the experimental wave was C_R^E m/s. Notice that this value is a constant in the optimization procedure that will be carried out, but its value is an unknown since it can not be obtained straight from the pictures but has to be deduced from the observed position of the experimental wave packet through time. In this section we will present a cost function that minimizes the distance between the numerical and experimental wave packets, in order to obtain from it not only a more accurate value for the Young modulus but also a good approximation for the experimental wave packet velocity.

Let us denote by x_0^N (resp. x_0^E) the position where the value of the amplitude of the numerical (resp. experimental) wave packet reaches its maximum at the first time instant in which the comparison is made. Due to the required pixels discretization in the experimental data it might not be possible to have $x_0^N = x_0^E$ so we will assume that there might be an initial gap between both such that

$$x_0^N = x_0^E + d.$$

Notice that, due to its definition, (see (15)), C_R^N depends on E and ν through the wavelength L and the relations in (6), so does the position of the numerical wave maximum at each time. This being the case, after t_i seconds, the position of both maxima, denoted by x_i^N and x_i^E respectively, will be:

$$x_i^N(E,\nu) = x_0^E + d + t_i C_R^N(E,\nu), \quad x_i^E = x_0^E + t_i C_R^E,$$

and given that $t_i = i\Delta t$, the difference between the position of the two maxima is

$$x_i^N(E,\nu) - x_i^E = d + i\Delta t(C_R^N(E,\nu) - C_R^E).$$

Now, summing over time (recall that we have $M = 135$ time steps for the experimental data), we obtain the minimization problem:

Find $(E^\star, \nu^\star)$ such that

$$\tilde{J}(E^\star,\nu^\star) = \min_{\substack{E\in\mathbb{R}^+ \\ \nu\in(0,1/2)}} \tilde{J}(E,\nu)$$

being

$$\tilde{J}(E,\nu) = \left(\sum_{i=1}^{M}(x_i^N(E,\nu) - x_i^E)^2\right)^{1/2}. \tag{31}$$

6.1.2. Dependance of C_R on E and ν

In this section we will study the dependence of the phase velocity on E and ν in order to decide which one affects the velocity the most. First, we recall some of the relations between wave parameters (see [30]):

$$C_R = c_t\xi, \quad E = \frac{C_R^2}{\xi^2}\rho_0 2(1+\nu). \tag{32}$$

From the second equation one can see that the value of the phase velocity depends only on the density ρ_0, the Young modulus E and the Poisson coefficient ν (since ξ only depends on ν, see [26]). The value of the density does not present any uncertainty, so once we obtain a good approximation of C_R with the optimization algorithm, we can compute E known ν, or ν given E. In order to decide which one has the strongest influence on the value of C_R, in this section we consider a given value for $C_R = 3000$ m/s, which is around of the expected value as we deduce from the wavelength approximation given in Section 3.2.1 and, starting from reference values of $E = 7.73e10$ Pa and $\nu = 0.34$ study how C_R varies when we change E and ν a certain range. This range of variation for E and ν has been set to 6% since this range applied to ν will imply a totally different material. As shown in Fig. 10, the six percent variation of ν gives a maximum of 0.5% variation of C_R (see blue line) while a six percent variation of E gives a 3% variation of C_R (see red dashed-dotted line). In consequence, the most critical parameter is the Young modulus.

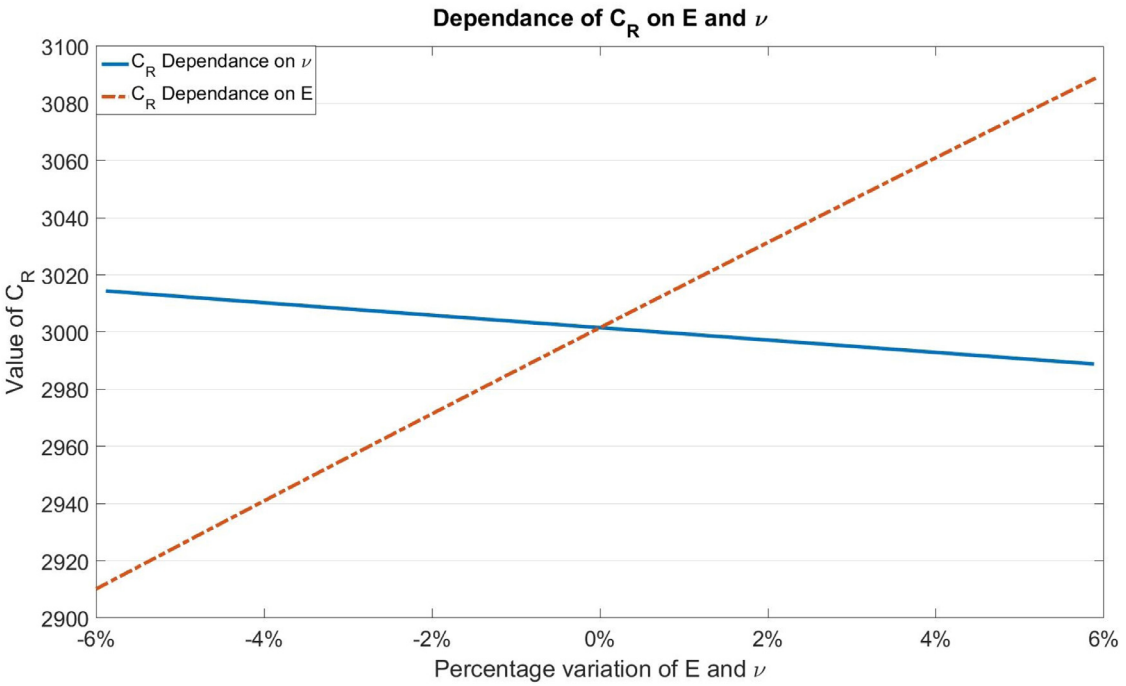

Fig. 10. Variation of C_R with respect to E and ν. (For interpretation of the references to color in this figure, the reader is referred to the web version of this article.)

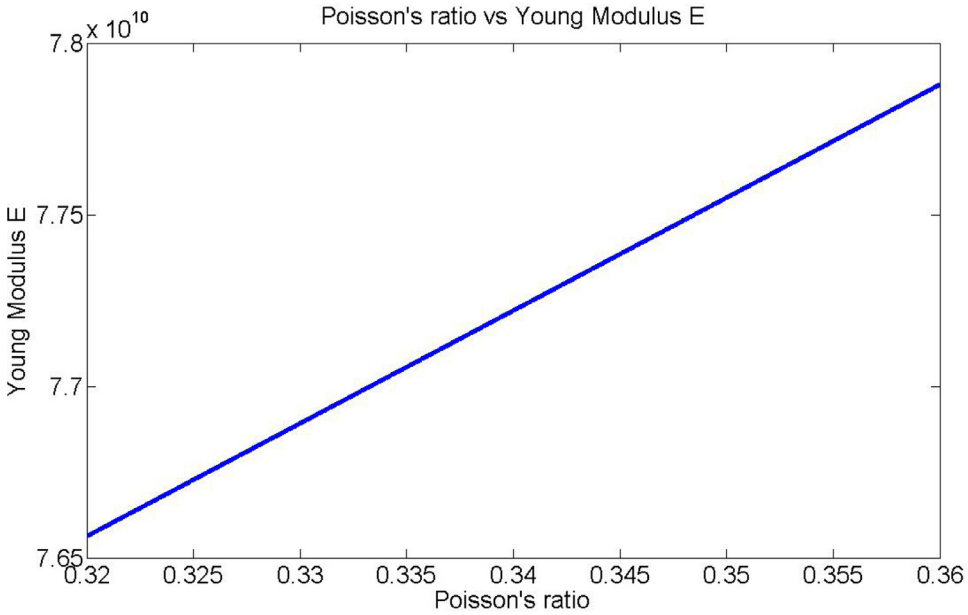

Fig. 11. Variation of E with respect to ν.

6.1.2.1. Error induced on E *by possible error on* ν. We know that the amplitude of the wave only depends on ξ, which also depends only on ν (see [26]). Besides, the expression of the Rayleigh waves is known except for a constant and the amplitude of the experimental wave packet has been normalized to RGB color values. Therefore, we can not know from this fact if the Poisson coefficient, ν, is correct. In order to limit the error on approximating E, we study now how a $\pm 6\%$ error margin on ν would affect the value of E. We consider as reference the provided value $\nu = 0.34$, and compute the values of ξ and E for $\nu \in [0.32, 0.36]$. In Fig. 11 we see that a 6% error on ν induces at most a 0.8% error on E, so we can consider $\nu = 0.34$, the value provided by the company, and get the value for E with less than one percent error.

Summing up, we will consider the initially provided value for $\nu = 0.34$ and the goal is to obtain the optimal $E^\star$ that minimizes the cost function $\tilde{J}(E, 0.34)$ defined in (34).

6.1.3. Steps of the algorithm

After the previous study we can now write the cost function (31) just in terms of E, considering $\nu = 0.34$. Notice that (31) can be expressed in terms of wave velocities as,

$$\tilde{J}(E, 0.34) = \left(\sum_{i=1}^{M} (d + i\Delta t (C_R^N(E, 0.34) - C_R^E))^2 \right)^{1/2}. \tag{33}$$

For simplicity we consider its square, and by using the known sum of the first M integers and their squares, we get the second order equation

$$\begin{aligned} J(E) := (\tilde{J}(E, 0.34))^2 = Md^2 + 2d\Delta t (C_R^N(E) - C_R^E) \frac{M(M+1)}{2} \\ + \Delta t^2 (C_R^N(E) - C_R^E)^2 \frac{M(M+1)(2M+1)}{6}, \end{aligned} \tag{34}$$

where for simplicity the evaluation at $\nu = 0.34$ is not explicit.

Now we summarize the steps of the algorithm to obtain the accurate material parameters, which will consist of the following steps:

1. Given an arbitrary Young modulus E_{j-1}, compute $C_R^N(E_{j-1})$ through expression (32).
2. Using the numerical procedure described in Section 5, solve the wave propagation problem with this data and compute $x_i^N(E_{j-1})$, $1 \le i \le M$.
3. Compute the numerical cost function associated, $J(E_{j-1})$ by using (31).
4. Solve the second order equation (34) and compute $I_{j-1} = C_R^N(E_{j-1}) - C_R^E$, which is the difference in the velocities of both wave packets.
5. Deriving (34) and using the computed value of I_{j-1}, $J'(E_{j-1})$ can be computed, from which we get the new value for E_j by applying a Newton method.
6. Update the material data and iterate from step 1 until convergence.
7. Once the convergence is achieved, update the material parameters according to (32).

Let us take a closer look at step 5. From the analytical expression in (34) we can get $J'(E)$ as

$$J'(E) = 2d\Delta t \frac{d(C_R^N(E))}{dE} \frac{M(M+1)}{2} + 2\Delta t^2 I \frac{d(C_R^N(E))}{dE} \frac{M(M+1)(2M+1)}{6},$$

being $I = C_R^N(E) - C_R^E$ and

$$\frac{dC_R^N(E)}{dE} = \frac{\xi}{\sqrt{\rho_0 2(1+\nu)}} \frac{1}{2\sqrt{E}}.$$

Therefore, with the target of computing the value for E such that it achieves the minimum value of J, Md^2, we apply a Taylor formula of first order to J:

$$J(E_j) = Md^2 \simeq J(E_{j-1}) + J'(E_{j-1})(E_j - E_{j-1}), \tag{35}$$

and then the value E_j to be used in the next iteration is obtained by approximating

$$Md^2 = J(E_{j-1}) + J'(E_{j-1})(E_j - E_{j-1}).$$

6.1.4. Stopping criteria

In this section, we briefly comment on the stopping criteria considered for the previous algorithm in the sixth step. To that end, we study the influence of the discretization in the computation of the cost function and the wave velocities. In particular, we can point out the following margins for the computation of J:

- First, the discrete maximum does not have to match the continuous one. We can only assure that both belong to the same pixel in the space interval. This translates to the phase velocities. In fact, we can compute the minimum difference between C_R^N and C_R^E to be numerically noticeable. This would be the case of a final gap between both maximum of half pixel. Being the observation time interval $T_f = 135 \times 2.e-7$ s and one pixel length $h = \frac{0.1107}{1023}$ m we have that the minimum observable difference in velocities is given by

$$C_R^N - C_R^E = \frac{h}{2T_f} = 2.0039 \text{ m/s}.$$

  So, if the difference between the numerical wave phase velocity and the experimental one is smaller than 2.0039 m/s we will not be able to appreciate any difference between them. This gives a first criteria for stopping the algorithm, when the difference between the phase velocities associated to two consecutive iterants, E_j and E_{j-1} is smaller than 2 m/s.

Table 2
Iterations of the optimization algorithm.

Young modulus E [Pa]	Phase velocity [m/s]	Numerical cost function
8.7859e10	3200	2.133e-03
8.1265e10	3077.5807	3.199e-04
7.8853e10	3031.5675	5.290e-05
7.7925e10	3013.6674	1.022e-05
7.7534e10	3006.0916	2.35e-06
7.7456e10	3004.5769	1.62e-06
7.7276e10	3001.0850	6.8e-07
7.7159e10	2999.8216	7.1e-07

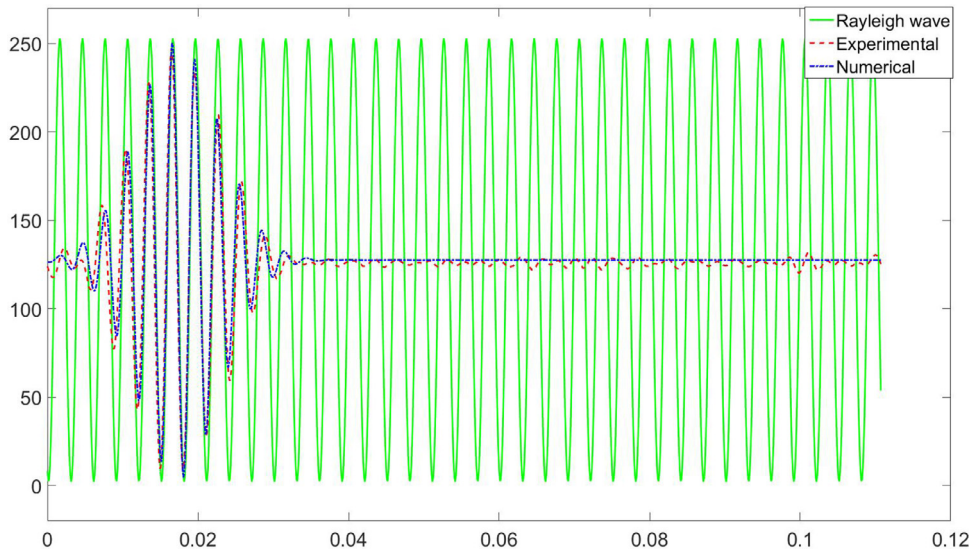

Fig. 12. Theoretical, numerical and experimental waves comparison at time $4\Delta t$. The abscissas axis represent the x direction and the ordinate the RGB value for each pixel. (For interpretation of the references to color in this figure, the reader is referred to the web version of this article.)

- Besides, due to the discrete data, when the maximum of the wave is reached inside an interval, the numerical and experimental waves might differ on which interval bound reaches the bigger value, so even if both waves are travelling exactly at the same velocity, we should consider a possible initial distance $d = h$ between x_0^N and x_0^E, and $Md^2 = 135\mathrm{h}^2 = 1.5808e-06$ m as the minimum value for the experimental cost function (even though $d = 0$ is also possible). Therefore, another stopping criteria for the algorithm will be

$$|J(E) - 1.5808e-06| \leq \epsilon. \tag{36}$$

Therefore, the algorithm will stop when the cost function is small enough and the difference between the velocities in two consecutive iterations is smaller than 2 m/s.

We can study the influence on E of this 2.0039 m/s error margin that we have in the optimization of $C_R^N(E)$. The expression of E in terms of phase velocity, period, frequency, density and Poisson coefficient is

$$E = \frac{C_R^2 T_0^2 f^2 \rho (1+\nu)}{\xi^2},$$

so, given the data of the experiment and a possible error of 2.0039 m/s in C_R^N we get a relative error for E of order $O(10^{-3})$. Therefore, with this procedure we can get E with less than one per mille.

6.2. Numerical results for the optimization procedure

In this section we show the numerical results for the algorithm introduced above.

In Table 2 we show the results for an optimization starting with Young modulus 8.7859e10 Pa and we can see that in seven iterations we get convergence. Notice that even if the cost function in step 6 is already small enough, the difference between the phase velocities associated to steps 5 and 6 is not, while both stopping criteria are met on the next step. So, with these results, we take as optimum $E^* = 7.7159e10$ Pa.

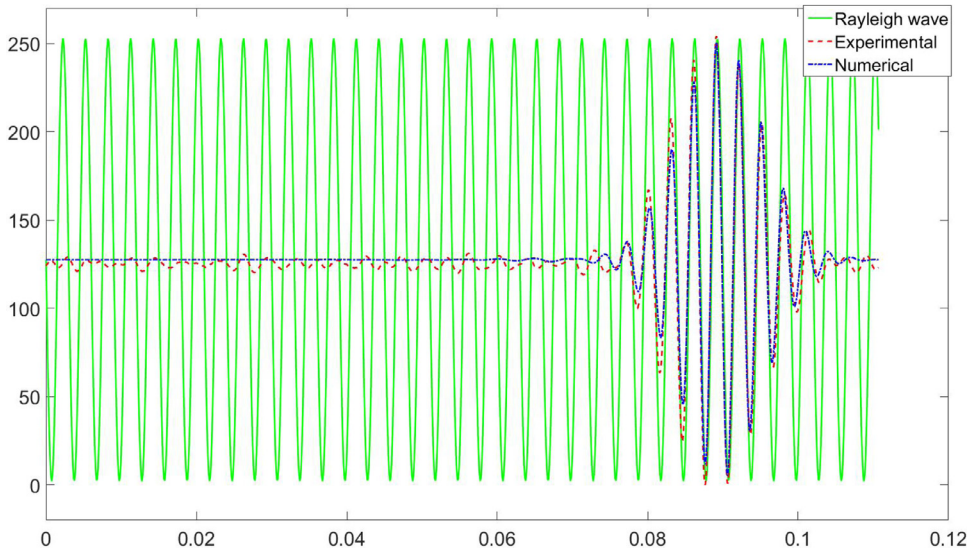

Fig. 13. Theoretical, numerical and experimental waves comparison at time $125\Delta t$. The abscissas axis represent the x direction and the ordinate the RGB value for each pixel. (For interpretation of the references to color in this figure, the reader is referred to the web version of this article.)

Remember that in Section 4.2 we have measured the wavelength from the experimental data which gave the approximate value $L = 0.003$ whose associated phase velocity is $C_R = 3000\,\text{m/s}$. The value provided by the numerical optimization agrees with this value since the difference between both velocities is just $0.1784\,\text{m/s}$, much smaller than $2.0039\,\text{m/s}$.

6.3. Final comparison

Once the data have been adjusted, we use them on the numerical simulation and both the numerical and experimental waves matched perfectly. On Figs. 12 and 13 we can see the comparison between the theoretical Rayleigh wave results with constant amplitude (green solid line), the numerical wave packet (red dashed line) and the experimental one (blue dash dotted line) at two different time steps. We can notice the good match on the waves amplitude as well as the lack of gap when the time passes, so both wave packet travel at the same speed. Therefore, both the material parameters values and the methodology used for their obtention are validated.

7. Conclusions

A mathematical model representing a Rayleigh wave packet has been introduced by obtaining the appropriate boundary and initial conditions to reproduce the provided experimental data.

The performance of the experimental data has been analyzed in order to compute the input data for the numerical model.

A finite element method has been developed and implemented to numerically replicate the experimental results.

An optimization procedure to accurately obtain the Young modulus of a given material has been provided, by computing the phase velocities of Rayleigh wave packets traveling on a sample plate.

The results of the numerical simulation considering the optimal values obtained have been compared with the experimental data obtaining good results.

Acknowledgements

The authors would like to acknowledge the cooperation of the members of the Optical Metrology research Group of the Applied Physics Department of the University of Vigo who provided the experimental data for this work as long as their input and experience on the matter.

This work was partially supported by FEDER and Xunta de Galicia funds under the ED431C 2017/60 grant, by the Ministry of Economy, Industry and Competitiveness through the Plan Nacional de I+D+i (MTM2015-68275-R).

References

[1] D. Pandey, S. Pandey, Ultrasonics: a technique of material characterization, in: D. Dissanayake (Ed.), Acoustic Waves, InTech, 2010, doi:10.5772/10153.
[2] D.B. Fraser, R.C. Lecraw, Novel method of measuring elastic and anelastic properties of solids, Rev. Sci. Instrum. 35 (9) (1964) 1113–1115.
[3] J. Plesek, R. Kolman, M. Landa, Using finite element method for the determination of elastic moduli by resonant ultrasound spectroscopy, J. Acoust. Soc. Am. 116 (1) (2004) 282–287.

[4] J.S. Popovics, W. Song, J.D. Achenbach, J.H. Lee, R.F. Andre, One-sided stress wave velocity measurement in concrete, J. Eng. Mech. 124 (12) (1998) 1346–1353.
[5] L. Qixian, J.H. Bungey, Using compression wave ultrasonic transducers to measure the velocity of surface waves and hence determine dynamic modulus of elasticity for concrete, Constr. Build. Mater. 10 (4) (1996) 237–242.
[6] T. Wu, J. Fang, A new method for measuring in situ concrete elastic constants using horizontally polarized conical transducers, J. Acoust. Soc. Am. 101 (1) (1997) 330–336.
[7] T. Wu, J. Fang, G. Liu, M. Kuo, Determination of elastic constants of a concrete specimen using transient elastic waves, J. Acoust. Soc. Am. 98 (4) (1995) 2142–2148.
[8] A. Bayón, F. Gascón, F.J. Nieves, Estimation of dynamic elastic constants from the amplitude and velocity of Rayleigh waves, J. Acoust. Soc. Am. 117 (6) (2005) 3469–3477, doi:10.1121/1.1898663.
[9] R. Medina, A. Bayón, Elastic constants of a plate from impact-echo resonance and Rayleigh wave velocity, J. Sound Vib. 329 (11) (2010) 2114–2126.
[10] F. Masoumi, A. Ghasemi-Ghalebahman, M. Kokabi, Identification of mechanical and damage parameters of composite laminates based on a CPAM method, J. Reinf. Plast. Compos. 37 (17) (2018) 1114–1128.
[11] F. Barra, V. Pagneux, J. Zuiga, Diffusive transport of waves in a periodic waveguide, Phys. Rev. E Stat. Nonlinear Soft Matter Phys. 85 (1) (2012). Cited By 6. doi: 10.1103/PhysRevE.85.016209.
[12] V. Pagneux, A. Maurel, Lamb wave propagation in elastic waveguides with variable thickness, Proc. R. Soc. A Math. Phys. Eng. Sci. 462 (2068) (2006) 1315–1339. Cited By 50. doi: 10.1098/rspa.2005.1612.
[13] V. Pagneux, Revisiting the edge resonance for lamb waves in a semi-infinite plate, J. Acoust. Soc. Am. 120 (2) (2006) 649–656. Cited By 37. doi: 10.1121/1.2214153.
[14] D. Royer, E. Dieulesaint, Elastic Waves in Solids, vol I and II, Advanced texts in physics, Springer, 2000.
[15] A. Abd-Alla, S. Abo-Dahab, H. Hammad, Propagation of Rayleigh waves in generalized magneto-thermoelastic orthotropic material under initial stress and gravity field, Appl. Math. Model. 35 (6) (2011) 2981–3000, doi:10.1016/j.apm.2010.11.067.
[16] S. Biswas, S. Abo-Dahab, Effect of phase-lags on Rayleigh wave propagation in initially stressed magneto-thermoelastic orthotropic medium, Appl. Math. Model. 59 (2018) 713–727, doi:10.1016/j.apm.2018.02.025.
[17] Z. Mustansar, A. Shaukat, L. Margetts, Effect of using different types of methods for the derivation of elastic modulus of bone - a critical survey, MATEC Web Conf. 108 (2017) 13002, doi:10.1051/matecconf/201710813002.
[18] K.S. Randhawa, The measurement of the Young's modulus of ice with ultrasonic waves, Ph.D. thesis, Konstruktion und Festigkeit von Schiffen M-10, 2018.
[19] X. Sun, S. Li, X. Dun, D. Li, T. Li, R. Guo, M. Yang, A novel characterization method of piezoelectric composite material based on particle swarm optimization algorithm, Appl. Math. Model. 66 (2019) 322–331, doi:10.1016/j.apm.2018.08.015.
[20] A. Bezza, P. Destuynder, C. Fabre, O. Wilk, Energy methods for non-destructive testing in a two dimensional damaged structure, Appl. Math. Model. 60 (2018) 300–319, doi:10.1016/j.apm.2018.03.029.
[21] E.H. Saenger, G.K. Kocur, R. Jud, M. Torrilhon, Application of time reverse modeling on ultrasonic non-destructive testing of concrete, Appl. Math. Model. 35 (2) (2011) 807–816, doi:10.1016/j.apm.2010.07.035.
[22] I. Iturrioz, G. Lacidogna, A. Carpinteri, Experimental analysis and truss-like discrete element model simulation of concrete specimens under uniaxial compression, Eng. Fract. Mech. 110 (2013) 81–98. Cited By 13. doi: 10.1016/j.engfracmech.2013.07.011.
[23] I. Iturrioz, G. Lacidogna, A. Carpinteri, Acoustic emission detection in concrete specimens: experimental analysis and lattice model simulations, Int. J. Damage Mech. 23 (3) (2014) 327–358. Cited By 32. doi: 10.1177/1056789513494232.
[24] S. Invernizzi, G. Lacidogna, A. Carpinteri, Particle-based numerical modeling of AE statistics in disordered materials, Meccanica 48 (1) (2013) 211–220. Cited By 11. doi: 10.1007/s11012-012-9595-5.
[25] M. Cao-Rial, C. Moreno, P. Quintela, A numerical-experimental non destructive technique for material characterisation, in: Libro de comunicaciones definitivas presentadas en CEDYA+CMA 2017, 2018. ISBN 978-84-944402-1-2.
[26] M.T. Cao, C. Moreno, P. Quintela, Simulation of Rayleigh waves in cracked plates, Math. Methods Appl. Sci. 30 (1) (2007) 15–42, doi:10.1002/mma.774.
[27] P. Rodríguez-Gómez, J.C. López-Vázquez, C. Trillo, A.F. Doval, J.L. Fernández, Transient elastic wave propagation and scattering in plates: comparison between pulsed TV-holography measurements and finite element method predictions, in: Proceedings Volume 8413, Speckle 2012: V International Conference on Speckle Metrology, 2012, doi:10.1117/12.977644.
[28] J. Deán, C. Trillo, A. Doval, J. Fernández, in: Video visualization of the dispersive behaviour of Rayleigh and lamb wavetrains by double-pulsed TV holography, 7098, 2008. Cited By 2. doi: 10.1117/12.803003.
[29] T.J. Hughes, The finite element method. Linear Static and Dynamic Finite Element Analysis, Prentice-Hall, 1987.
[30] M.T. Cao-Rial, Problemas de contacto en elasticidad dinámica con XFEM, (Ph.D. thesis, USC,), 2011.